Journal Pre-proofs

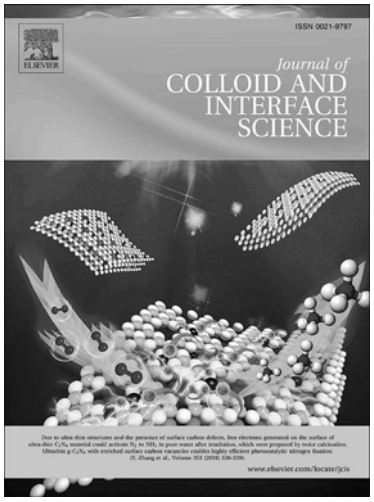

Self-Assembled Nanostructure Induced in Deep Eutectic Solvents via an Amphiphilic Hydrogen Bond Donor

Joshua J. Buzolic, Hua Li, Zachary Aman, Gregory G. Warr, Rob Atkin

PII: S0021-9797(22)00253-3
DOI: https://doi.org/10.1016/j.jcis.2022.02.029
Reference: YJCIS 29762

To appear in: *Journal of Colloid and Interface Science*

Received Date: 17 January 2022
Revised Date: 1 February 2022
Accepted Date: 6 February 2022

Please cite this article as: J.J. Buzolic, H. Li, Z. Aman, G.G. Warr, R. Atkin, Self-Assembled Nanostructure Induced in Deep Eutectic Solvents via an Amphiphilic Hydrogen Bond Donor, *Journal of Colloid and Interface Science* (2022), doi: https://doi.org/10.1016/j.jcis.2022.02.029

Self-Assembled Nanostructure Induced in Deep Eutectic Solvents via an Amphiphilic Hydrogen Bond Donor

Joshua J. Buzolic [a], Hua Li [a,b], Zachary Aman [c], Gregory G. Warr [d], Rob Atkin [a*]

[a] *School of Molecular Sciences, The University of Western Australia, Perth, WA, 6009, Australia*
[b] *Centre for Microscopy, Characterisation and Analysis, The University of Western Australia, Perth, WA, 6009, Australia*
[c] *Centre for Long Subsea Tiebacks, The University of Western Australia, Perth, WA, 6009, Australia*
[d] *School of Chemistry and Sydney Nano Institute, The University of Sydney, Sydney, NSW, 2006, Australia*

Hypothesis: Popular deep eutectic solvents (DESs) typically lack amphiphilic molecules and ions and therefore do not have the useful self-assembled nanostructures prevalent in many ionic liquids. We hypothesise that nanostructure in DESs can be induced via an amphiphilic hydrogen bond donor (HBD), and that nanostructure becomes better defined with HBD chain length.
Experiments: The structure of DESs formed from choline chloride mixed with either butyric acid (ChCl/BuOOH) or hexanoic acid (ChCl/HeOOH) in a 1:4 molar ratio were studied using atomic force microscopy (AFM) imaging, force curves, and friction measurements combined with bulk rheology.
Findings: DESs formed with both the C_4 and C_6 acids are nanostructured. As the length of the acid group is increased from C_4 to C_6, AFM images reveal the nanostructure becomes larger and better defined due to the longer acid chain, and AFM force curves show the interfacial nanostructure extends further from the surface. Self-assembled nanostructure in these systems is a consequence of choline cations, chloride anions, and acid alcohol groups clustering together due to electrostatic attractions and hydrogen bonding to form polar domains. Acid alkyl chains are solvophobically excluded from the polar domains and aggregate into apolar domains.

Key words: nanostructure, amphiphilic, atomic force microscopy, friction, deep eutectic solvents

*Corresponding author

Abbreviations: DESs, deep eutectic solvents; HBD, hydrogen bond donor; ChCl, choline chloride; BuOOH, butyric acid; HeOOH, hexanoic acid; AFM, atomic force microscopy; DFT, density functional theory; MD, molecular dynamics; ILs, ionic liquids; AM-AFM, amplitude modulation atomic force microscopy; 2D FFT, two-dimensional fast Fourier transform; A_0, free amplitude; A, set amplitude; A/A_0, amplitude setpoint ratio; μ, friction coefficient; η, viscosity; $\dot{\gamma}$, shear rate.

E-mail addresses: rob.atkin@uwa.edu.au (R. Atkin)

1. Introduction

Deep eutectic solvents (DESs) are mixtures of a salt and a hydrogen bond donor (HBD) in a specific molar ratio which forms a homogenous liquid phase with melting point lower than the individual components [1], and usually (but not always) lower than the expected effect of freezing point

depression. The molar ratio which results in the lowest melting point is the eutectic composition, although many studies of DESs may also occur at other nearby compositions. The first reported DES comprised choline chloride (ChCl, m.p. = 302 °C) and urea (m.p. = 135 °C) in a 1:2 molar ratio [1,2]. To date, the DESs that have attracted the most research interest are composed of ChCl mixed with either urea (reline), ethylene glycol (ethaline), glycerol (glyceline), malic acid, or oxalic acid [3–5].

Hydrogen bonding is critical for the formation and properties of DESs. Density Functional Theory (DFT) calculations show that an "alphabet soup of many different types of hydrogen bonds" occurs between the choline chloride and urea in reline [6]. The properties of the hydrogen bond network regulate the magnitude of the DES melting point depression and viscosity [6]. Inelastic neutron scattering in combination with *ab initio* calculations revealed that soft and strong interactions impart flexibility to the hydrogen bond network in reline that contribute to the melting point depression [7]. DFT calculations [8] and neutron diffraction [9] studies have also confirmed the structure, stability, and behaviour of common DESs are a consequence of hydrogen bonding between the HBD and the chloride anion, and choline and chloride ions. Molecular dynamics (MD) simulations of reline, ethaline, and glyceline found that differences between hydrogen bond interactions lead to the different eutectic temperatures and viscosities [10]. MD simulations of ChCl mixed with derivatives of urea found that altering the HBD type changes interactions between the chloride anions and the HBD alkyl chains [11]. DFT calculations of DESs composed of ChCl with carboxylic acid HBDs showed varying the alkyl chain length affects the solute-solvent interactions and physicochemical properties of DESs, including polarity and charge transfer [12].

DESs are closely related to the much more extensively studied class of ionic liquids (ILs) with the main point of difference being that ILs are pure salts in a liquid state with no added HBD. ILs with sufficiently long alkyl chains tend to form sponge-like nanostructures in the bulk liquid. Attractive interactions between charged moieties lead to the formation of polar domains of anions and cation head groups, which solvophobically exclude cation alkyl chains into apolar domains [13]. This amphiphilic nanostructure leads to many useful properties, such as the ability to dissolve both polar and apolar compounds simultaneously [13]. ILs are highly tuneable, but many are toxic and require expensive starting materials [14]. DESs exhibit many of the useful properties of ILs, notably tunability and low vapor pressure, but can be made from cheaper, non-toxic and biodegradable materials. However, typical DESs lack any species with amphiphilic characteristics, so are not nanostructured in that there are not separate polar and apolar domains [13]. Amphiphilic DESs that combine IL nanostructure with these cheaper, greener materials are therefore of interest.

We have used neutron diffraction to show that nanostructure can be induced in DESs through the amphiphilic cation via mixing glycerol with either ethylammonium bromide, propylammonium bromide, or butylammonium bromide [13]. In these DESs, the polar domain is composed of the cation ammonium group, bromide, and glycerol, while the non-polar domain is formed by the cation alkyl chains [13]. As in ILs [15], increasing the cation alkyl chain length amplifies the solvophobic effect, resulting in better-defined and larger nanostructure, and changing the HBD to urea alters the nanostructure [13,16]. A small angle neutron scattering study of the conformation of poly(ethylene) oxide dissolved in alkylammonium DESs showed increasing the cation alkyl chain length reduces the density of hydrogen bonding sites, which decreases the solvent quality for the polymer [17]. The structure of DESs at solid/liquid interfaces has been investigated by atomic force microscopy (AFM) and other interfacial methods. AFM studies have shown that at a charged graphite surface, chloride and choline are attracted into the Stern layer at positive and negative potentials, respectively [18]. For DESs with amphiphilic cations, the longer alkyl chains lead to stronger alkyl chain association at interfaces, as in the bulk [19]. Addition of water to DESs has, surprisingly, led to stronger interfacial nanostructure up to ~40 wt% water, which is attributed to the water molecules solvating and swelling the DES structure, and participating in the hydrogen bond network [20]. Above 50 wt% the ions and HBD are solvated which weakens intermolecular interactions, and interfacial nanostructure is reduced

[21,22]. This is in stark contrast to ILs where addition of small amounts of water decreases interfacial nanostructure [20]. A combined AFM and simulation study of the interface of glycerine with graphite and mica surfaces has emerged and shown interfacial nanostructure varies with surface type [23]. Scanning tunnelling microscopy [24], surface force balance [25], neutron reflectometry [26], electrochemical studies [27–31], MD simulations [32–36], and DFT simulations [37] have also been used to probe solid DES interfaces. The main finding of these studies is that the surface charge is the main factor in determining which DES components are enriched in the Stern layer, except at neutral potential [32].

The hypothesis for this work is that nanostructure can be induced in DESs by using amphiphilic HBDs, instead of an amphiphilic cation, and that this nanostructure can be detected at the mica/DES interface. DESs formed from terpenes and monocarboxylic acids have been studied previously using phase diagrams, viscosities and solvatochromic dyes, [38] but the possibility of amphiphilic nanostructure was not explored or postulated. In this study, the amphiphilic HBDs, butyric acid (BuOOH) and hexanoic acid (HeOOH), are mixed with choline chloride, the archetypical DES salt. These DESs liquids combine the nanostructure typical of ionic liquids with the low cost, green properties of DESs. This study enables the influence of HBD alkyl chain length on interfacial nanostructure to be explored using AFM imaging, as well as normal and lateral (friction) force measurements. The outcomes will provide a new pathway for rational design of DES nanostructure towards applications, such as low-cost biodegradable lubricants.

2. Materials and Methods

2.1. Materials

Choline chloride (Sigma, >98%), butyric acid (Sigma-Aldrich, >99%), and hexanoic acid (Aldrich, >99%) were used as received. Mica substrates were obtained from SPI Supplies (V-1 Grade, 15 mm).

2.2. Sample Preparation

Choline chloride was mixed with either butyric acid or hexanoic acid in a 1:4 molar ratio, heated at 60 °C and stirred at 600 rpm until a clear, homogenous liquid phase formed. The samples were sealed with Parafilm to minimise exposure to air. The residual water content of the samples was on average 0.42 wt% from Karl-Fischer titration measurements.

2.3. AFM Experiments

A Veeco Nanoscope IV AFM was used to measure normal force vs separation curves and lateral (frictional) force vs normal load curves on a freshly cleaved mica surface. Sharp silicon AFM tips (NSC36, Mikromasch) with spring constants of $0.7 \pm 0.3 N^{-1}$ were cleaned with ethanol and MilliQ water, followed by UV-Ozone for 10 min before use. The AFM fluid cell (Bruker) was washed with ethanol followed by MilliQ water and dried with nitrogen flow before experiment. Normal force *vs* separation curves were collected by moving the surface towards the AFM tip and detecting the cantilever deflection as a function of separation. The ramp size ranged from 50 nm to 100 nm and ramp rate was 0.2 Hz. Standard methods were used to convert deflection vs separation data to normal force vs separation curves. Lateral forces were obtained by performing AFM scans with a scan angle of 90° (with respect to the long axis of the cantilever) and with the slow scan axis disabled. The scan size was 500 nm, and scan rate was 6 Hz. The lateral deflection signal (i.e. cantilever twist) was converted to lateral force using a customised function produced in MATLAB, which takes into account the torsional spring constant and the geometrical dimensions of the cantilever [39]. Every experiment was repeated at least three times on different areas of the surface.

Amplitude modulation AFM (AM-AFM) *in situ* imaging of a mica surface immersed in both DESs was conducted using the Cypher VRS AFM (Asylum Research) at different temperatures to determine the impact that temperature has on interfacial structure. 40 °C was found to be the optimal temperature to image interfacial structure, as any attempts to image below 40 °C were unsuccessful due to choline

chloride precipitation. Feature in AFM images changed as expected with scan sizes and scan angles, making image artefacts unlikely. The cantilever tips used for imaging have a reported spring constant of either 6.0 Nm^{-1} or 0.09 Nm^{-1}; this is to optimise the opportunity to observe features in either the Stern layer or the near-surface layer. Using a stiffer spring enables the AFM tip to disrupt and reach the surface more easily, whereas using a softer spring means that the AFM tip cannot reach the surface easily and will only interact with the near-surface layer**.** All images were taken after the system stabilised and were collected over a period of 1-4 h. Any vertical measurements using AFM images will be slightly inaccurate, due to the image stretching that occurs from the tip moving across and down the selected area, and image analysis will therefore focus on horizontal measurements. AM-AFM imaging data was analysed to extract the repeat spacing of the surface features, by using two-dimensional Fast Fourier Transform (2D FFT) Integral Transformation with the radial profile and the Fit Function tools in the Gwyddion program, which specialises in AFM analysis [40]. The calculated repeat spacing value is used to determine the size of the structures of an image, which can be employed to determine the near-surface structure of the solvents on interfaces.

2.4. Rheology Experiments

Rheological measurements were conducted using a TA Instruments DHR-3 rheometer with attached Peltier plate. The geometry used was a 2° stainless steel cone with a diameter of 20 mm. For viscosity vs shear rate tests, the shear ramp swept from 1 s^{-1} to 1000 s^{-1} linearly over a 10 min period. For viscosity vs temperature tests, the temperature ramp swept from 60 °C (333 K) to 40 °C (313 K) at a fixed shear rate of 800 s^{-1}. All runs were performed in duplicate with replacement of the solvent between each run.

3. Results and Discussion

3.1. Force-Separation Profiles

Normal force-separation profiles for an AFM probe approaching a mica surface immersed in 1:1:4 Ch:Cl:BuOOH or 1:1:4 Ch:Cl:HeOOH, referred to as ChCl/BuOOH or ChCl/HeOOH respectively, at 40 °C are shown in **Fig. 1a** and **Fig. 1b**. The force curves shown best represent the key features of several hundred force curves collected over different days. A single representative force curve is presented rather than an average, as averaging can obscure common features at small normal forces, as described previously [18,41]. Additional exemplar force separation profiles can be found in **Fig. S1** and **Fig. S2** in SI, which are consistent with Fig. 1. In an AFM experiment, the absolute distance between the AFM tip and the surface cannot be determined as the compliance region (zero apparent separation) corresponds to probe pushing against material that cannot be displaced, and not necessarily contacting the surface. For a silica AFM tip and a mica substrate, steps in force profiles result from material being displaced from the mica surface rather than the silica tip [42,43]. This is because the silica AFM tip has lower charge density and is rougher than mica, which means that material silica tip will be displaced at lower force [42,43].

Previous work on DESs [18–20] and ILs [44–51] have shown that near smooth solid surfaces the liquid forms discrete layers, which produce steps in AFM force curves. The width of the steps is determined by physical size of the species enriched in a given layer. The number of steps (layers) and magnitude of push through forces depend on the level of order and lateral cohesive interactions within a layer. Generally, liquids with well ordered Stern layers and strong bulk nanostructure have strongly structured interfaces [18,19,52,53].

Key features in Fig. 1a and Fig. 1b are indicated by arrows. For ChCl/BuOOH in Fig. 1a, as the AFM tip approaches the surface from large separation, the measured force is zero. At an apparent separation of 1.3 nm a repulsion is detected, which increases monotonically to 4 nN at an apparent separation of 0.9 nm. At this point, there is an inward jump in the force-separation data, followed by push-through into compliance at a force of 3 nN. For ChCl/HeOOH in Fig. 1b, the distance at which the repulsion is

first sensed increases to 3.0 nm, after which there is a monotonic increase in force to 2.1 nm. This is followed by a short jump to a small step at 1.8 nm, then a second monotonic increase in force from 1.8 nm to 1.3 nm, and then a second short jump**.** Finally, there is a steep increase in force to 12 nN as the separation decreases to 0.9 nm and a more gentle compression force up to 16 nN at compliance.

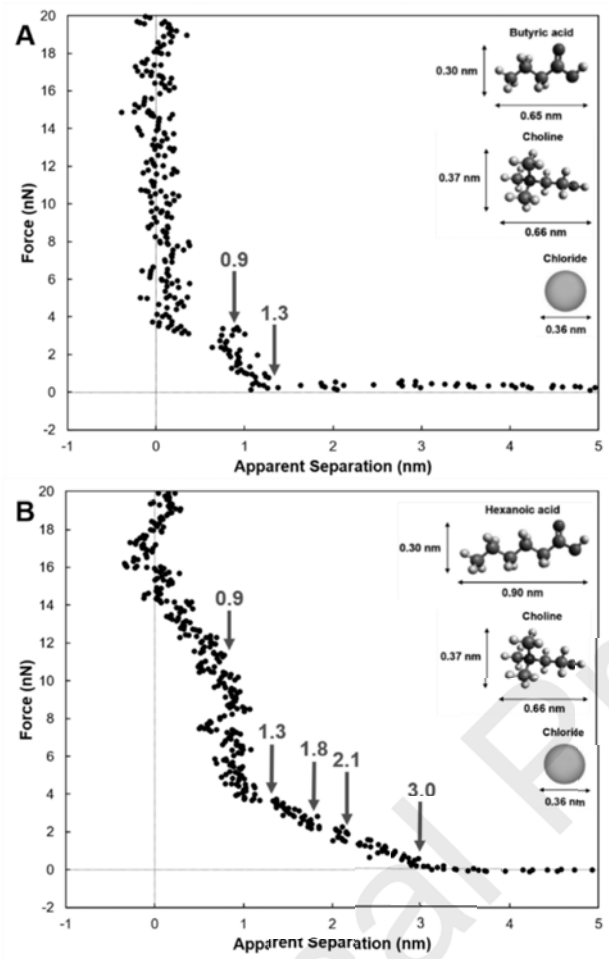

Fig. 1. Representative normal force-separation profiles of an AFM tip approaching mica immersed in ChCl/BuOOH (A) and in ChCl/HeOOH at 40 °C (B). Insets show the structure and dimensions of the respective carboxylic acids, choline, and chloride calculated using Avogadro software [49,54].

The large, near-surface step for ChCl/BuOOH has a width of 1.3 nm from the onset of repulsion to the end of the jump, which is too large to be due either to layers enriched in choline and chloride, which have previously been shown to be 0.3 to 0.5 nm thick [18], or a monomer layer of BuOOH, which has an extended length of 0.65 nm. However, 1.3 nm matches twice the extended length of BuOOH, consistent with these large near-surface steps due resulting from solvophobically self-assembled BuOOH aggregates. These acid aggregates form because the choline cations, chloride anions, and acid alcohol groups cluster together due to electrostatic attractions and hydrogen bonding to form polar domains, which exclude the acid alkyl chains into apolar domains. As the AFM tip pushes againt the aggregates, they are first compressed (1.3 nm to 0.9 nm) and then ruptured as the tip jumps to compliance, whereupon the AFM tip pushes against the cation-enriched Stern layer which it cannot displace [18].

A similar argument holds for ChCl/HeOOH. The longer alkyl chain for ChCl/HeOOH compared to ChCl/BuOOH leads to stronger lateral cohesion between neighbouring acid molecules within apolar regions. Consequently, rather than the compression and explusion observed for ChCl/BuOOH,

expulsion of HeOOH aggregates occurs via two 0.9 nm sublayers, first from 1.8 nm to 0.9 nm, then from 0.9 nm to compliance. The two steps immediately adjacent to the surface are both 0.9 nm wide, consistent with the extended length of HeOOH, so these steps are due to solvophobically self-assembled HeOOH aggregates atop a cation-enriched Stern layer which cannot be displaced at compliance [18]. The additional steps at 2.1 nm and wider distances are due to liquid nanostructures that are less well ordered but extend further from the surface.

The step widths found in Fig. 1 are significantly larger than those of DESs composed of ChCl mixed with conventional HBDs [18]. This is consistent with amphiphilic DESs featuring distinct polar and apolar domains, and therefore larger near-surface layers.

3.2. Images

Fig. 2a and **Fig. 2b** present 5 nm x 5 nm AFM phase images of near-surface nanostructure (above the Stern layer) at a mica surface for ChCl/BuOOH and ChCl/HeOOH, respectively. Phase rather than topography images are presented because differences in height are minimal, whereas differences in phase are more sensitive to the liquid compliance between the AFM tip and the surface, and thus reveal near-surface structures more clearly [55–57]. In Fig. 2, dark areas are compliant and bright areas are non-compliant, which can loosely be conceptualised as compressible and stiff, respectively, similar as seen before for nanostructured ILs [58]. All features scaled and rotated as expected as imaging parameters were changed and were reproduced in topographical images.

To obtain these images the cantilever is completely immersed in the DESs. A piezoelectric actuator is used to acoustically excite the cantilever, which oscillates at or near its resonant frequency with a user-determined amplitude. A photodiode and laser are used in combination to monitor the vertical motion of the cantilever with resolution less than an Ångström. As the oscillating tip nears the mica surface, the free amplitude (A_0) is dampened to the set amplitude (A), and the cantilever oscillation phase lags behind the input oscillation. A is kept approximately constant via a feedback loop, from which topographical and phase images are produced. The images for ChCl/BuOOH and ChCl/HeOOH were obtained using an amplitude setpoint ratio (A/A_0) > 0.6 [57].

Comparison of Fig. 2a and Fig. 2b reveals some similarities and stark differences. For ChCl/HeOOH, the image shows a well-defined, interconnected, sponge-like structure, with the distance between the centres of light (or dark) features of the order of a few nanometres. For ChCl/BuOOH, the near-surface structure is less well defined, and consists of smaller, irregular blobs with a spacing of 1 to 2 nm between the centres of corresponding areas. Structures in both images are too large to be due to Stern layer cations adsorbed to the mica, which typically form hexagonal rows aligned by the mica 0.52 nm apart [53]. This confirms that the images in Fig. 2a and Fig. 2b are of the near-surface structure, and not the Stern layer. The bright (non-compliant) areas in the image show the location of polar domains, where electrostatic and hydrogen bonding interactions between groups lead to a relatively rigid local structure, and the dark regions are the more compliant, apolar domains of self-assembled acid alkyl chains. Comparable near-surface nanostructures were observed previously for 1-butanol, 1-octanol and 1-dodecanol dissolved in the ionic liquid propylammonium nitrate at similar volume fractions [58], as well as bulk nanostructures of propylammonium nitrate, ethanolammonium nitrate, and ethylammonium nitrate [59,60].

The insets to Fig. 2 show phase image FFTs and radial profiles extracted from the FFT. The FFTs exhibit broad peaks consistent with the disordered images. The peak in the radial profile for ChCl/BuOOH is at 0.646 nm^{-1}, and for ChCl/HeOOH at 0.350 nm^{-1}, which correspond to real space repeat spacings of 1.6 nm and 2.9 nm, respectively. These values are larger than the aggregate sizes detected in the AFM normal force curves due to flattening of nanostructure structures by the smooth flat mica substrate, as per ionic liquids [61].

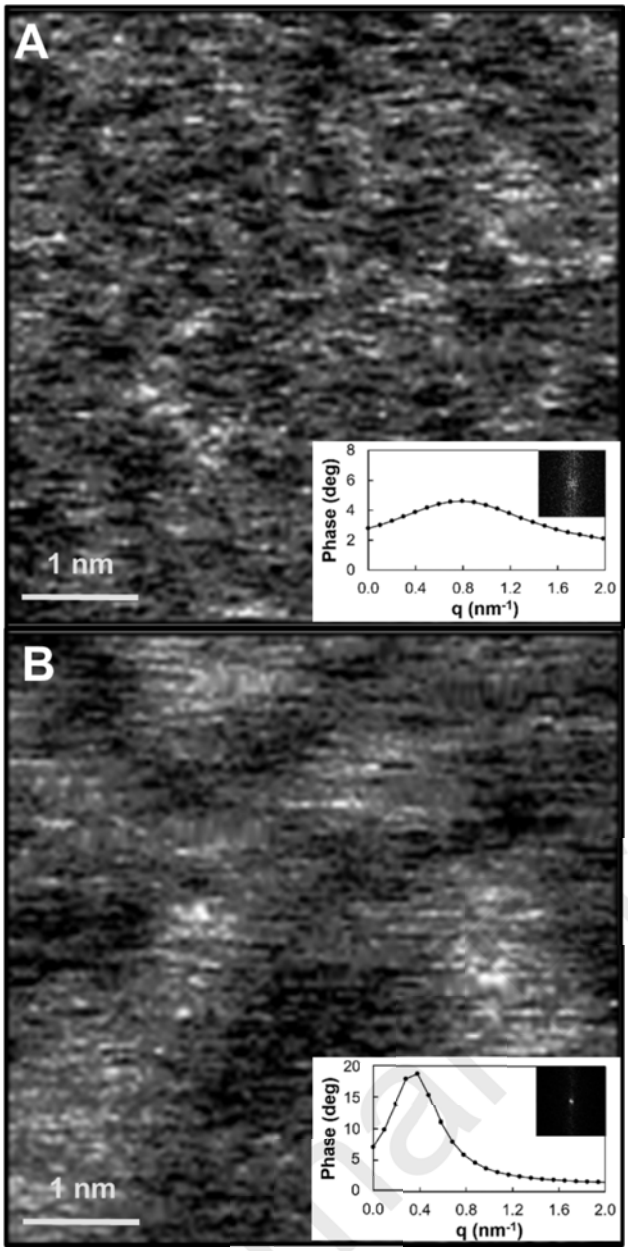

Fig. 2. 5 nm by 5 nm AM-AFM phase images of mica immersed in ChCl/BuOOH (A) and in ChCl/HeOOH at 40 °C (B). Insets show the 2D FFT image and radial average of the FFT.

Given that near-surface and bulk nanostructure are usually closely related [14]**,** the AFM images and force curves in combination provide compelling evidence that amphiphilic nanostructure in these DESs has been induced via the HBD. We have completed neutron diffraction measurements for ChCl/BuOOH, which reveal a low q pre-peak that confirms bulk nanostructure on the same length scale.

3.3. Friction

Fig. 3 shows lateral (frictional) force versus normal force of mica immersed in ChCl/BuOOH and ChCl/HeOOH, with air for comparison at the nanoscale. Nanofriction was measured instead of macrofriction because nanoscale friction studies are less affected by surface asperities and roughness than macroscale measurements, and thus can elucidate molecular scale lubrication effects critical for understanding the lubrication mechanism. For both DESs, two friction regimes are apparent, similar to previous studies on mica and other surfaces [62–65]. In the low normal force (multilayer) regime, the AFM tip is in contact with multiple layers near, but not bound to, the mica surface (i.e. the

near-surface layers). In the high normal force (boundary) regime, the AFM tip is in contact with the layer strongly bound to the mica surface (i.e. the Stern layer, referred to as the boundary layer in friction). The jump in lateral force for the two DESs are at the normal loads of 4 nN for ChCl/BuOOH and 15 nN for ChCl/HeOOH. This jump indicates the critical normal force (breakpoint), which delineates the transition from the multilayer regime to the boundary regime. The scheme in Fig. 3 illustrates this transition for ChCl/HeOOH on mica. The longer alkyl chain of HeOOH than BuOOH leads to stronger solvophobic interactions in the apolar domains, resulting in a stronger multilayer regime in ChCl/HeOOH than in ChCl/BuOOH, which is consistent with the force-separation curves (Fig. 1) and near surface layer imaging (Fig. 2). This means a higher normal load is required for the AFM tip to disrupt the multilayer regime for ChCl/HeOOH compared to ChCl/BuOOH. Studies of ethylammonium nitrate confined between mica and silica found the breakpoint was consistently between normal loads of 15 nN and 20 nN at different temperatures [62], which is consistent with the ChCl/HeOOH results. Both normal force values are in good agreement with the final push-through forces (3 nN and 16 nN, respectively) detected in the normal force curves in Fig. 1. The push-through to compliance in the force curves indicates the tip is now in contact with the Stern layer, which matches with the jump in the friction data indicating the tip is now in contact with the boundary layer.

In the multilayer regime, friction is affected by many factors, including adhesion and the near-surface layer structure. The friction coefficient (μ), which is the proportionality between the lateral force and the normal force, is higher for ChCl/HeOOH (0.20) than for ChCl/BuOOH (0.18) in the multilayer regime, mainly because ChCl/HeOOH has stronger near-surface layers, and more energy is dissipated when the AFM tip slides across and brushes aside these near-surface layers. In the boundary regime, the AFM tip is in contact with a strongly adsorbed ion layer. The friction coefficients are almost the same for ChCl/BuOOH and ChCl/HeOOH in the boundary regime and consistent with previous reported ChCl/ethylene glycol DES [25], whereas much smaller than that in air. In the boundary regime, the friction coefficient is mainly determined by the boundary layer composition. The similarity in friction coefficients for ChCl/BuOOH and ChCl/HeOOH together with ChCl/ethylene glycol strongly suggest that in the boundary regime, HBD molecules and chloride have been squeezed out for both systems, and the boundary layers are enriched in choline cations which are strongly bound with the negatively charged mica surface. These results are consistent with the normal force curves in Fig. 1, and with a choline cation enriched boundary layer remaining between the AFM tip and mica surface to increase lubricity. Further, the sudden jump in lateral force at the critical normal force is higher for ChCl/HeOOH (30 nN) than for ChCl/BuOOH (15 nN). Previous studies have shown this sudden jump is proportional to the energy dissipated to brush aside the ion layers adsorbed on top of the sliding plane [65–68]. In this study, as HeOOH has longer alkyl chain than BuOOH, the solvophobic interaction between the final HeOOH enriched near-surface layer and the underneath choline cation enriched boundary layer is stronger, thus requires more energy to brush aside the final near-surface layer.

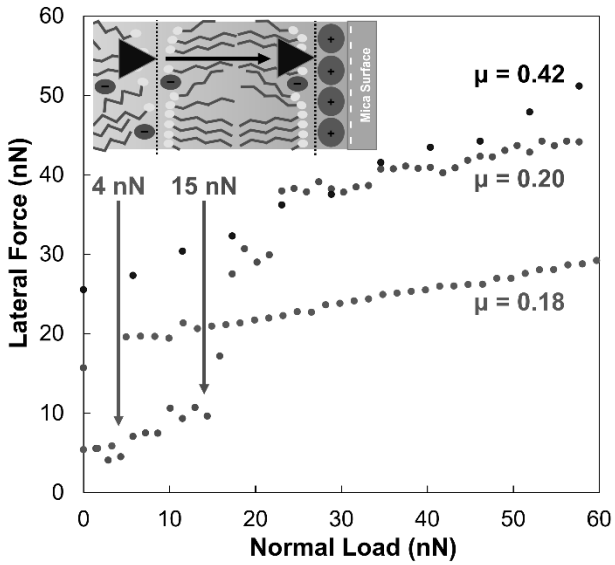

Fig. 3. Lateral force vs normal force of mica in air (black), ChCl/BuOOH (blue), and ChCl/HeOOH (red) at 40 °C. The friction coefficient, μ, is extracted from the gradient of the plot in the boundary regime. Inset shows representative schematic of the transition from the multilayer regime to the boundary regime for ChCl/HeOOH on mica.

3.4. Viscosity

Fig. 4 shows the viscosity (η) of ChCl/BuOOH and ChCl/HeOOH as a function of shear rate ($\dot{\gamma}$) at 313 K (red) and 333 K (blue), respectively. For all conditions investigated, shear-thinning is observed, where viscosity decreases as shear rate increases, indicating the non-Newtonian nature of the investigated DES systems. A log-log plot based on the same data as Fig. 4 can be found in **Fig. S3** in Supplementary Information, which further supports the shear-thinning properties of ChCl/BuOOH and ChCl/HeOOH. This is similar as seen before in studies of ChCl-based DESs and their aqueous mixtures [10,19], likely caused by disruption of hydrogen bond network and/or bulk nanostructure.

The inset of Fig. 4 shows the viscosity as a function of temperature at a fixed shear rate of 50 s^{-1} and the fits with the natural logarithmic form of the Arrhenius equation (**Eq. 1**):

$$\ln \eta = \ln \eta_{\infty} + \frac{E_{\eta}}{\mathrm{RT}} \qquad \text{(Eq. 1)}$$

where E_{η} is the activation energy for viscous flow, η_{∞} is the viscosity at infinite temperature, and R is the universal gas constant [69,70]. The fitted E_{η} is 21.2 kJ mol^{-1} for ChCl/HeOOH, which is 35% higher than that for ChCl/BuOOH (15.6 kJ mol^{-1}). This difference is likely due to the increased solvophobic segregation and better-defined nanostructure due to the longer alkyl chain of HeOOH compared to BuOOH. This results in a greater force needed to disrupt the interfacial layers, leading to higher energy barriers for the molecules and ions moving past each other under shear, which further shows the correlation between lubrication, friction, and normal force curves.

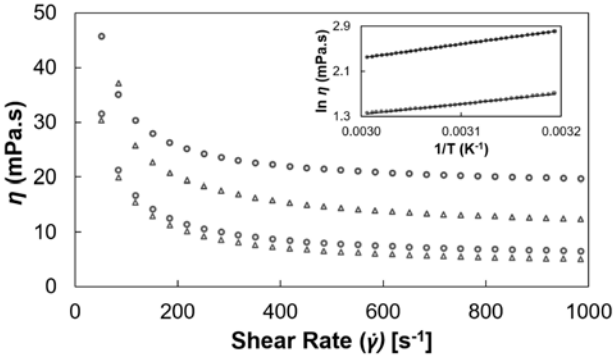

Fig. 4. Viscosity (η) as a function of shear rate ($\dot{\gamma}$) from 1 s^{-1} to 1000 s^{-1} for ChCl/BuOOH (blue) and ChCl/HeOOH (red), at 313 K (circles) and 333 K (triangles). Inset shows viscosity as a function of temperature at a fixed shear rate of 800 s^{-1} and fits to the Arrhenius equation.

4. Conclusions

Nanostructure in DESs has previously only been reported for amphiphilic cations, [13,16,71] that is, in the same way as for ionic liquids. In this work, we show that nanostructure in DESs can also be induced via amphiphilic HBDs. AFM imaging, force curves, and friction measurements have been used to study the interfacial properties of ChCl/BuOOH and ChCl/HeOOH. The results demonstrate that amphiphilic nanostructure can be induced in DESs by using intermediate chain length carboxylic acids as the hydrogen bond donor, and that this nanostructure becomes better defined as alkyl chain length increases. The force-separation profiles show the near-surface layers for ChCl/HeOOH extend further into the bulk compared to ChCl/BuOOH, due to the longer alkyl chain length of hexanoic acid. The near-surface structure seen in the AFM images features more distinct and larger structures for ChCl/HeOOH in contrast to ChCl/BuOOH. This is consistent with the longer alkyl chain of hexanoic acid forming larger apolar domains and a better-defined nanostructure due to the stronger solvophobic interactions. The friction data reveals that both solvents are lubricating, with ChCl/BuOOH showing better lubricating properties, despite ChCl/BuOOH being less viscous than ChCl/HeOOH. These results provide a new pathway for DESs in applications where liquid nanostructure is desirable, such as low-cost biodegradable lubricants.

CRediT authorship contribution statement

Joshua J. Buzolic: Methodology, Data curation, Formal analysis, Writing – original draft. **Hua Li:** Supervision, Methodology, Writing – review & editing. **Zachary Aman:** Methodology. **Gregory G. Warr:** Funding acquisition, Conceptualisation, Writing – review & editing. **Rob Atkin:** Supervision, Conceptualisation, Funding acquisition, Writing – review & editing.

Declaration of Competing Interest

The authors declare that they have no known competing financial interests or personal relationships that could have appeared to influence the work reported in this paper.

Acknowledgements

JB is support by an UWA RTP. This work was supported by ARC Discovery Projects (DP200102248). JB thanks Lucas Wong, Yunxiao Zhang, Justin Freeman, and Jianan Wang for helpful comments.

Appendix A. Supplementary Data

Supplementary data to this article can be found at [].

References

1. Abbott AP, Boothby D, Capper G, Davies DL, Rasheed RK. Deep Eutectic Solvents formed between choline chloride and carboxylic acids: Versatile alternatives to ionic liquids. J Am Chem Soc. 2004;126(29):9142–7.

2. García G, Atilhan M, Aparicio S. In silico rational design of ionic liquids for the exfoliation and dispersion of boron nitride nanosheets. Phys Chem Chem Phys. 2015;18(2):1212–24.

3. Hansen BB, Spittle S, Chen B, Poe D, Zhang Y, Klein JM, Horton A, Adhikari L, Zelovich T, Doherty BW, Gurkan B, Maginn EJ, Ragauskas A, Dadmun M, Zawodzinski TA, Baker GA, Tuckerman ME, Savinell RF, Sangoro JR. Deep Eutectic Solvents: A Review of Fundamentals and Applications. Chem Rev. 2021;121(3):1232–85.

4. Jablonský M, Škulcová A, Kamenská L, Vrška M, Šima J. Deep Eutectic Solvents: Fractionation of Wheat Straw. BioResources. 2015;10(4):8039–47.

5. Zhang CW, Xia SQ, Ma PS. Facile pretreatment of lignocellulosic biomass using deep eutectic solvents. Bioresour Technol [Internet]. 2016;219:1–5. Available from: http://dx.doi.org/10.1016/j.biortech.2016.07.026

6. Ashworth CR, Matthews RP, Welton T, Hunt PA. Doubly ionic hydrogen bond interactions within the choline chloride-urea deep eutectic solvent. Phys Chem Chem Phys. 2016;18(27):18145–60.

7. Araujo CF, Coutinho JAP, Nolasco MM, Parker SF, Ribeiro-Claro PJA, Rudić S, Soares BIG, Vaz PD. Inelastic neutron scattering study of reline: Shedding light on the hydrogen bonding network of deep eutectic solvents. Phys Chem Chem Phys. 2017;19(27):17998–8009.

8. Gautam R, Kumar N, Lynam JG. Theoretical and experimental study of choline chloride-carboxylic acid deep eutectic solvents and their hydrogen bonds. J Mol Struct. 2020;1222:128849.

9. Hammond OS, Bowron DT, Edler KJ. Liquid structure of the choline chloride-urea deep eutectic solvent (reline) from neutron diffraction and atomistic modelling. Green Chem. 2016;18(9):2736–44.

10. Stefanovic R, Ludwig M, Webber GB, Atkin R, Page AJ. Nanostructure, hydrogen bonding and rheology in choline chloride deep eutectic solvents as a function of the hydrogen bond donor. Phys Chem Chem Phys. 2017;19(4):3297–306.

11. Shayestehpour O, Zahn S. Molecular Features of Reline and Homologous Deep Eutectic Solvents Contributing to Nonideal Mixing Behavior. J Phys Chem B. 2020;124(35):7586–97.

12. Dwamena AK, Raynie DE. Solvatochromic Parameters of Deep Eutectic Solvents: Effect of Different Carboxylic Acids as Hydrogen Bond Donor. J Chem Eng Data. 2020;65(2):640–6.

13. McDonald S, Murphy T, Imberti S, Warr GG, Atkin R. Amphiphilically Nanostructured Deep Eutectic Solvents. J Phys Chem Lett. 2018;9(14):3922–7.

14. Hayes R, Warr GG, Atkin R. Structure and Nanostructure in Ionic Liquids. Chem Rev. 2015;115(13):6357–426.

15. Hayes R, Imberti S, Warr GG, Atkin R. Effect of cation alkyl chain length and anion type on protic ionic liquid nanostructure. J Phys Chem C. 2014;118(25):13998–4008.

16. Brunner M, Imberti S, Warr GG, Atkin R. Liquid Structure of Single and Mixed Cation Alkylammonium Bromide Urea Deep Eutectic Solvents. J Phys Chem B. 2020;124(39):8651–64.

17. Chen Z, McDonald S, FitzGerald P, Warr GG, Atkin R. Small angle neutron scattering study of the conformation of poly(ethylene oxide) dissolved in deep eutectic solvents. J Colloid Interface Sci. 2017;506:486–92.

18. Chen Z, McLean B, Ludwig M, Stefanovic R, Warr GG, Webber GB, Page AJ, Atkin R. Nanostructure of Deep Eutectic Solvents at Graphite Electrode Interfaces as a Function of Potential. J Phys Chem C. 2016;120(4):2225–33.

19. Chen Z, Ludwig M, Warr GG, Atkin R. Effect of cation alkyl chain length on surface forces and physical properties in deep eutectic solvents. J Colloid Interface Sci. 2017;494:373–9.

20. Hammond OS, Li H, Westermann C, Al-Murshedi AYM, Endres F, Abbott AP, Warr GG, Edler KJ, Atkin R. Nanostructure of the deep eutectic solvent/platinum electrode interface as a function of potential and water content. Nanoscale Horizons. 2019;4(1):158–68.

21. Dai Y, Witkamp GJ, Verpoorte R, Choi YH. Tailoring properties of natural deep eutectic solvents with water to facilitate their applications. Food Chem [Internet]. 2015;187:14–9. Available from: http://dx.doi.org/10.1016/j.foodchem.2015.03.123

22. Hammond OS, Bowron DT, Jackson AJ, Arnold T, Sanchez-Fernandez A, Tsapatsaris N, Garcia Sakai V, Edler KJ. Resilience of Malic Acid Natural Deep Eutectic Solvent Nanostructure to Solidification and Hydration. J Phys Chem B. 2017;121(31):7473–83.

23. Elbourne A, Meftahi N, Greaves TL, McConville CF, Bryant G, Bryant SJ, Christofferson AJ. Nanostructure of a deep eutectic solvent at solid interfaces. J Colloid Interface Sci. 2021;591:38–51.

24. Tan Z, Peng Y, Liu J, Yang Y, Zhang Z, Chen Z, Mao B, Yan J. An In Situ Scanning Tunneling Microscopy Study on the Electrochemical Interface between Au(111) and Ethaline Deep Eutectic Solvent. ChemElectroChem. 2020;7(22):4601–5.

25. Hallett JE, Hayler HJ, Perkin S. Nanolubrication in deep eutectic solvents. Phys Chem Chem Phys. 2020;22(36):20253–64.

26. Zec N, Mangiapia G, Zheludkevich ML, Busch S, Moulin JF. Revealing the interfacial nanostructure of a deep eutectic solvent at a solid electrode. Phys Chem Chem Phys. 2020;22(21):12104–12.

27. Wu J, Zhou R, Radjenovic PM, Liu S, Wu D, Li J, Mao B, Yan J. Electrochemical impedance spectroscopy and Raman spectroscopy studies on electrochemical interface between Au(111) electrode and ethaline deep eutectic solvent. Electrochim Acta [Internet]. 2021;390:138859. Available from: https://doi.org/10.1016/j.electacta.2021.138859

28. Figueiredo M, Gomes C, Costa R, Martins A, Pereira CM, Silva F. Differential capacity of a deep eutectic solvent based on choline chloride and glycerol on solid electrodes. Electrochim Acta. 2009;54(9):2630–4.

29. Dean W, Klein J, Gurkan B. Do Deep Eutectic Solvents Behave Like Ionic Liquid Electrolytes? A Perspective from the Electrode-Electrolyte Interface. J Electrochem Soc. 2021;168(2):026503.

30. Fuchs D, Bayer BC, Gupta T, Szabo GL, Wilhelm RA, Eder D, Meyer JC, Steiner S, Gollas B.

Electrochemical Behavior of Graphene in a Deep Eutectic Solvent. ACS Appl Mater Interfaces. 2020;12(36):40937–48.

31. Vieira L, Schennach R, Gollas B. In situ PM-IRRAS of a glassy carbon electrode/deep eutectic solvent interface. Phys Chem Chem Phys. 2015;17(19):12870–80.

32. Mamme MH, Moors SLC, Terryn H, Deconinck J, Ustarroz J, De Proft F. Atomistic Insight into the Electrochemical Double Layer of Choline Chloride-Urea Deep Eutectic Solvents: Clustered Interfacial Structuring. J Phys Chem Lett. 2018;9(21):6296–304.

33. Mamme MH, Moors SLC, Mernissi Cherigui EA, Terryn H, Deconinck J, Ustarroz J, De Proft F. Water distribution at the electrified interface of deep eutectic solvents. Nanoscale Adv. 2019;1(8):2847–56.

34. Gao Q, Wu N, Qin Y, Laaksonen A, Zhu Y, Ji X, Lu X. Molecular insight into wetting behavior of deep eutectic solvent droplets on ionic substrates: A molecular dynamics study. J Mol Liq [Internet]. 2020;319:114298. Available from: https://doi.org/10.1016/j.molliq.2020.114298

35. Rozas S, Atilhan M, Aparicio S. Deep Eutectic Solvent Reline at 2D Nanomaterial Interfaces. J Phys Chem B. 2020;124(7):1197–206.

36. Atilhan M, Aparicio S. Molecular dynamics simulations of mixed deep eutectic solvents and their interaction with nanomaterials. J Mol Liq [Internet]. 2019;283:147–54. Available from: https://doi.org/10.1016/j.molliq.2019.03.068

37. Atilhan M, Costa LT, Aparicio S. Elucidating the Properties of Graphene-Deep Eutectic Solvents Interface. Langmuir. 2017;33(21):5154–65.

38. Martins MAR, Crespo EA, Pontes PVA, Silva LP, Bülow M, Maximo GJ, Batista EAC, Held C, Pinho SP, Coutinho JAP. Tunable Hydrophobic Eutectic Solvents Based on Terpenes and Monocarboxylic Acids. ACS Sustain Chem Eng. 2018;6(7):8836–46.

39. Schwarz UD, Köster P, Wiesendanger R. Quantitative analysis of lateral force microscopy experiments. Rev Sci Instrum. 1996;67(7):2560–7.

40. Wydro MJ, Warr GG, Atkin R. Amplitude-modulated atomic force microscopy reveals the near surface nanostructure of surfactant sponge (L3) and lamellar (Lα) phases. Langmuir. 2015;31(19):5513–20.

41. McLean B, Li H, Stefanovic R, Wood RJ, Webber GB, Ueno K, Watanabe M, Warr GG, Page A, Atkin R. Nanostructure of [Li(G4)] TFSI and [Li(G4)] NO3 solvate ionic liquids at HOPG and Au(111) electrode interfaces as a function of potential. Phys Chem Chem Phys. 2015;17(1):325–33.

42. Atkin R, Warr GG. Structure in confined room-temperature ionic liquids. J Phys Chem C. 2007;111(13):5162–8.

43. Werzer O, Cranston ED, Warr GG, Atkin R, Rutland MW. Ionic liquid nanotribology: Mica-silica interactions in ethylammonium nitrate. Phys Chem Chem Phys. 2012;14(15):5147–52.

44. Griffin LR, Browning KL, Clarke SM, Smith AM, Perkin S, Skoda MWA, Norman SE. Direct measurements of ionic liquid layering at a single mica–liquid interface and in nano-films between two mica–liquid interfaces. Phys Chem Chem Phys. 2017;19(1):297–304.

45. Perkin S, Crowhurst L, Niedermeyer H, Welton T, Smith AM, Gosvami NN. Self-assembly in the

electrical double layer of ionic liquids. Chem Commun. 2011;47(23):6572–4.

46. Smith AM, Lovelock KRJ, Perkin S. Monolayer and bilayer structures in ionic liquids and their mixtures confined to nano-films. Faraday Discuss. 2013;167:279–92.

47. Smith AM, Lovelock KRJ, Gosvami NN, Licence P, Dolan A, Welton T, Perkin S. Monolayer to bilayer structural transition in confined pyrrolidinium-based ionic liquids. J Phys Chem Lett. 2013;4(3):378–82.

48. Beattie DA, Espinosa-Marzal RM, Ho TTM, Popescu MN, Ralston J, Richard CJE, Sellapperumage PMF, Krasowska M. Molecularly-thin precursor films of imidazolium-based ionic liquids on mica. J Phys Chem C. 2013;117(45):23676–84.

49. Espinosa-Marzal RM, Arcifa A, Rossi A, Spencer ND. Ionic liquids confined in hydrophilic nanocontacts: Structure and lubricity in the presence of water. J Phys Chem C. 2014;118(12):6491–503.

50. Zhang R, Han M, Ta K, Madsen KE, Chen X, Zhang X, Espinosa-Marzal RM, Gewirth AA. Potential-Dependent Layering in the Electrochemical Double Layer of Water-in-Salt Electrolytes. ACS Appl Energy Mater. 2020;3(8):8086–94.

51. Jurado LA, Espinosa-Marzal RM. Insight into the Electrical Double Layer of an Ionic Liquid on Graphene. Sci Rep. 2017;7(1):1–12.

52. Horn RG, Evans DF, Ninham BW. Double-layer and solvation forces measured in a molten salt and its mixtures with water. J Phys Chem. 1988;92(12):3531–7.

53. Elbourne A, Voïtchovsky K, Warr GG, Atkin R. Ion structure controls ionic liquid near-surface and interfacial nanostructure. Chem Sci. 2015;6(1):527–36.

54. Hanwell MD, Curtis DE, Lonie DC, Vandermeerschd T, Zurek E, Hutchison GR. Avogadro: An advanced semantic chemical editor, visualization, and analysis platform. J Cheminform. 2012;4(8):1–17.

55. Elbourne A, McDonald S, Voïchovsky K, Endres F, Warr GG, Atkin R. Nanostructure of the Ionic Liquid-Graphite Stern Layer. ACS Nano. 2015;9(7):7608–20.

56. Voïtchovsky K, Kuna JJ, Contera SA, Tosatti E, Stellacci F. Direct mapping of the solid-liquid adhesion energy with subnanometre resolution. Nat Nanotechnol. 2010;5(6):401–5.

57. McDonald S, Elbourne A, Warr GG, Atkin R. Metal ion adsorption at the ionic liquid-mica interface. Nanoscale [Internet]. 2016;8(2):906–14. Available from: http://dx.doi.org/10.1039/c5nr05833c

58. Elbourne A, Cronshaw S, Voïtchovsky K, Warr GG, Atkin R. Near surface properties of mixtures of propylammonium nitrate with n-alkanols 1. Nanostructure. Phys Chem Chem Phys. 2015;17(40):26621–8.

59. Murphy T, Callear SK, Warr GG, Atkin R. Dissolved chloride markedly changes the nanostructure of the protic ionic liquids propylammonium and ethanolammonium nitrate. Phys Chem Chem Phys. 2016;18(26):17169–82.

60. Atkin R, Warr GG. The smallest amphiphiles: Nanostructure in protic room-temperature ionic liquids with short alkyl groups. J Phys Chem B. 2008;112(14):4164–6.

61. Hayes R, Warr GG, Atkin R. At the interface: solvation and designing ionic liquids. Phys Chem

Chem Phys [Internet]. 2010;12(8):1648–1648. Available from: 10.1039/B920393A

62. Hjalmarsson N, Atkin R, Rutland MW. Is the boundary layer of an ionic liquid equally lubricating at higher temperature? Phys Chem Chem Phys. 2016;18(13):9232–9.

63. Li H, Atkin R, Page AJ. Combined friction force microscopy and quantum chemical investigation of the tribotronic response at the propylammonium nitrate-graphite interface. Phys Chem Chem Phys. 2015;17(24):16047–52.

64. Hjalmarsson N, Atkin R, Rutland MW. Effect of Lithium Ions on Rheology and Interfacial Forces in Ethylammonium Nitrate and Ethanolammonium Nitrate. J Phys Chem C. 2016;120(47):26960–7.

65. Sweeney J, Webber GB, Rutland MW, Atkin R. Effect of ion structure on nanoscale friction in protic ionic liquids. Phys Chem Chem Phys. 2014;16(31):16651–8.

66. Elbourne A, Sweeney J, Webber GB, Wanless EJ, Warr GG, Rutland MW, Atkin R. Adsorbed and near-surface structure of ionic liquids determines nanoscale friction. Chem Commun. 2013;49(60):6797–9.

67. Li H, Niemann T, Ludwig R, Atkin R. Effect of Hydrogen Bonding between Ions of like Charge on the Boundary Layer Friction of Hydroxy-Functionalized Ionic Liquids. J Phys Chem Lett. 2020;11(10):3905–10.

68. Li H, Cooper PK, Somers AE, Rutland MW, Howlett PC, Forsyth M, Atkin R. Ionic liquid adsorption and nanotribology at the silica-oil interface: Hundred-fold dilution in oil lubricates as effectively as the pure ionic liquid. J Phys Chem Lett. 2014;5(23):4095–9.

69. Ziyada AK, Wilfred CD. Effect of Cation Modification on the Physicochemical Properties and CO2 Solubility: Nonfluorinated Phosphonium-Based Ionic Liquids Incorporating a Dioctylsulfosuccinate Anion. J Chem Eng Data. 2018;63(10):3672–83.

70. Okoturo OO, VanderNoot TJ. Temperature dependence of viscosity for room temperature ionic liquids. J Electroanal Chem. 2004;568(1–2):167–81.

71. Chen Z, Greaves TL, Warr GG, Atkin R. Mixing cations with different alkyl chain lengths markedly depresses the melting point in deep eutectic solvents formed from alkylammonium bromide salts and urea. Chem Commun. 2017;53(15):2375–7.

Figures

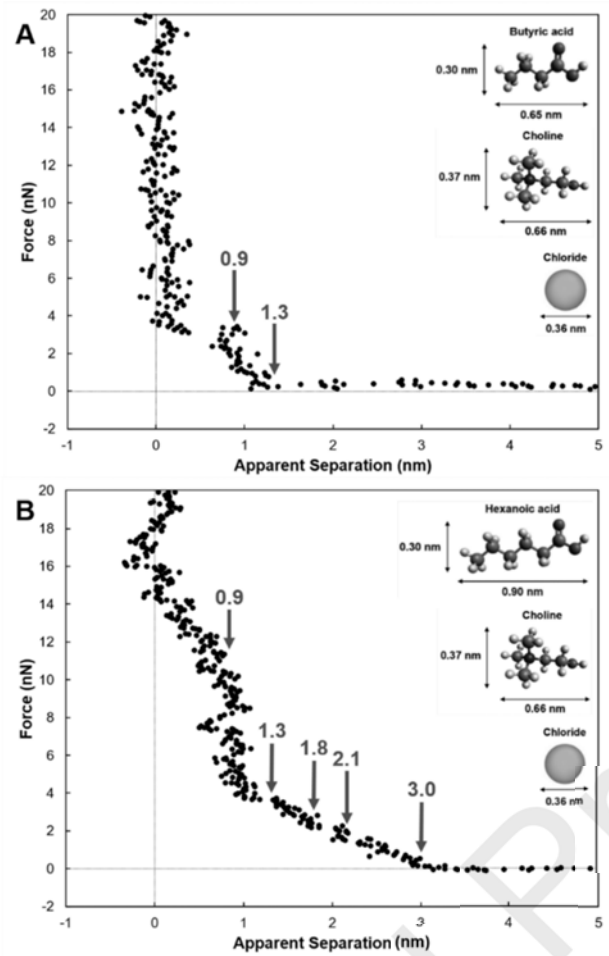

Fig. 1. Representative normal force-separation profiles of an AFM tip approaching mica immersed in ChCl/BuOOH (A) and in ChCl/HeOOH at 40 °C (B). Insets show the structure and dimensions of the respective carboxylic acids, choline, and chloride calculated using Avogadro software [49,54].

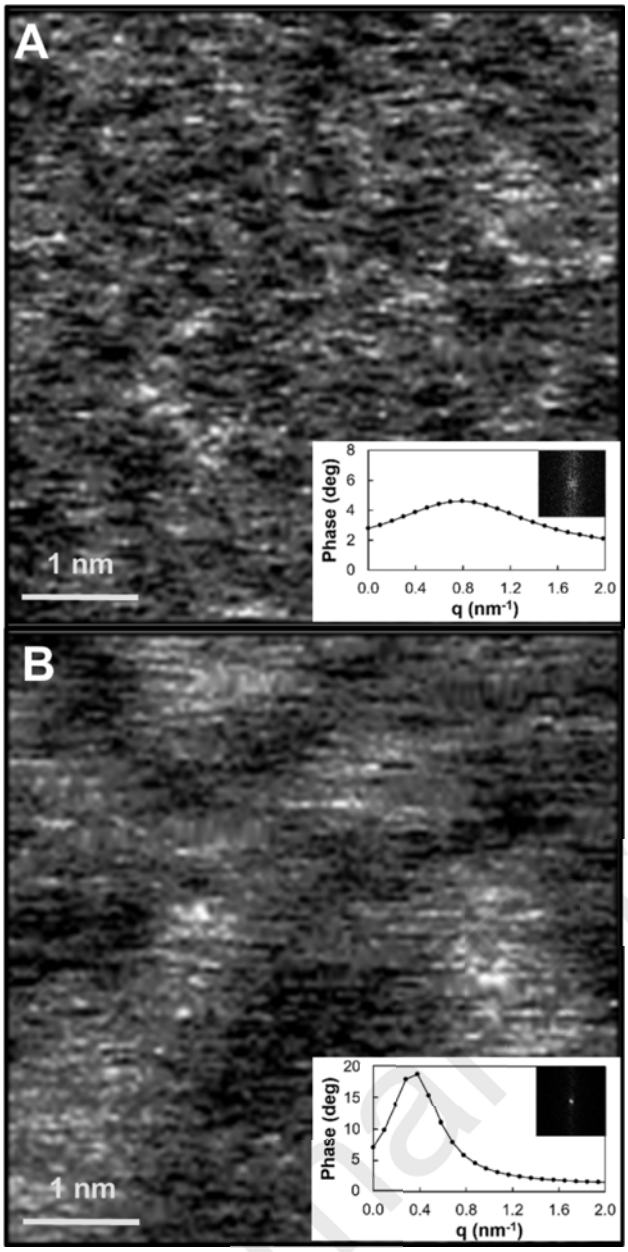

Fig. 2. 5 nm by 5 nm AM-AFM phase images of mica immersed in ChCl/BuOOH (A) and in ChCl/HeOOH at 40 °C (B). Insets show the 2D FFT image and radial average of the FFT.

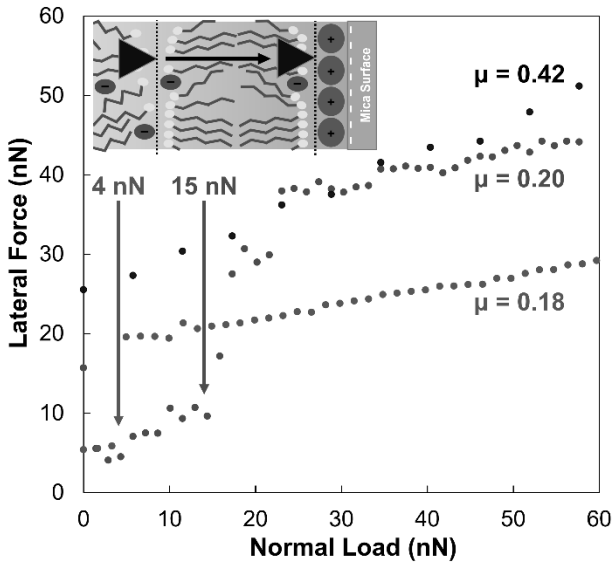

Fig. 3. Lateral force vs normal force of mica in air (black), ChCl/BuOOH (blue), and ChCl/HeOOH (red) at 40 °C. The friction coefficient, μ, is extracted from the gradient of the plot in the boundary regime. Inset shows representative schematic of the transition from the multilayer regime to the boundary regime for ChCl/HeOOH on mica.

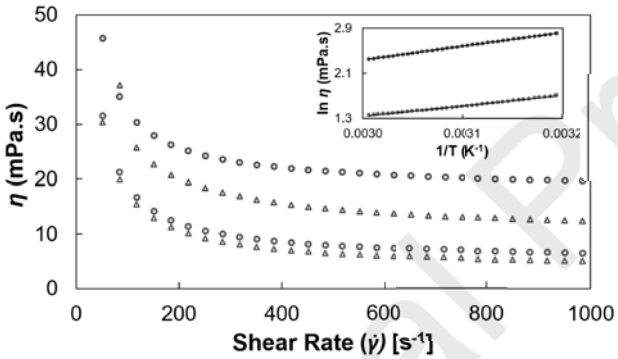

Fig. 4. Viscosity (η) as a function of shear rate ($\dot{\gamma}$) from 1 s^{-1} to 1000 s^{-1} for ChCl/BuOOH (blue) and ChCl/HeOOH (red), at 313 K (circles) and 333 K (triangles). Inset shows viscosity as a function of temperature at a fixed shear rate of 800 s^{-1} and fits to the Arrhenius equation.

1 Graphical abstract

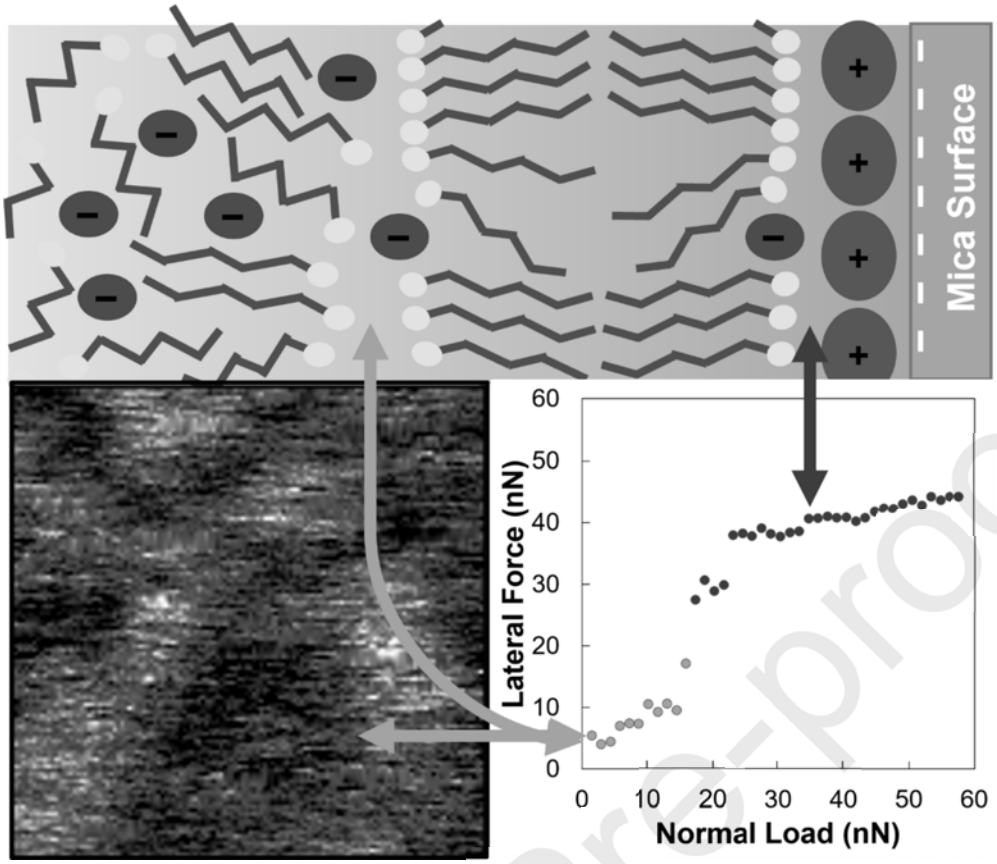

2

3

CRediT authorship contribution statement

Joshua J. Buzolic: Methodology, Data curation, Formal analysis, Writing – original draft. **Hua Li:** Supervision, Methodology, Writing – review & editing. **Zachary Aman:** Methodology. **Gregory G. Warr:** Funding acquisition, Conceptualisation, Writing – review & editing. **Rob Atkin:** Supervision, Conceptualisation, Funding acquisition, Writing – review & editing.

Declaration of interests

☒ The authors declare that they have no known competing financial interests or personal relationships that could have appeared to influence the work reported in this paper.

☐The authors declare the following financial interests/personal relationships which may be considered as potential competing interests: